X-Ray Spectroscopic Measurements of Areal Density and Modulations of Compressed Shells in Implosion Experiments on OMEGA

Introduction

In inertial confinement fusion (ICF), spherical targets are driven either directly with laser beams[1] or indirectly with x-ray drive.[2] Initial target nonuniformities, either existing or created by the drive, can grow because of hydrodynamic instabilities disrupting the implosion and reducing its thermonuclear yield.[3] Therefore, it is important to measure the effects of these instabilities on the target performance and particularly on the shell integrity. Fusion reactions occur during the stagnation phase, at peak compression, when the maximum density and temperature are achieved. Simultaneously, the hot core and the inner surface of the shell emit most of their radiation in x rays.[3] This emission not only contains information about important parameters such as areal density, temperature, and their uniformity in the region from where the emission originates (hot core and inner shell), but can also be used to probe the rest of the cold shell.[4] While the shell's final areal density, neutron yield, and core temperature are important parameters of the target performance, the shell's integrity provides a more direct signature of instability.

Cold-shell integrity has been measured for shells with Ti-doped layers.[5] Monochromatic core images were obtained at energies below and above the *K*-edge energy of Ti with a pinhole-array x-ray spectrometer.[6] The ratio between such images reflects the nonuniformity of the cold shell; however, these measurements were limited to implosions with 20-μm-thick shells and 1-ns square pulse shape, which had the highest-intensity x-ray emission from the core. Slowly rising pulse shapes and thicker shells produce implosions with lower core intensity. When measured with a pinhole-array spectrometer, this intensity was insufficient to perform meaningful analysis.

In the present experiments the sensitivity of the measurements is increased by replacing the diffracting crystal in the pinhole-array spectrometer with filters for sampling the spectrum below and above the Ti *K* edge. This allows for measurements of shell integrity for 20- and 24-μm-thick shells with both the 1-ns square pulse shape and a slower-rising, 2.3-ns pulse that has a 1:6 foot-to-main-pulse intensity ratio (PS26). Pure CH targets were used to measure nouniformities in radiation temperature and uniformity of the emitting (hot) part of the target, which consists of the core and inner part of the shell.

In this article three measurement methods are described: (1) Imaging of the cold-shell modulations is based on the imaging of core radiation in two x-ray energies, absorbed and nonabsorbed by the shell. The ratio of intensities in the two narrow-energy-band x-ray images is used to infer modulation in the areal density of the absorbing shell. (2) Measurements of temperature nonuniformities in the core radiation use core images from two energy bands, both unattenuated by the shell. (3) Imaging of the hot-shell modulations measures emission nonuniformities at x-ray energies unattenuated by the shell. Since most of this emission comes from the inner, hot shell, the modulations in the images are related to the hot shell's areal-density nonuniformities.

Experiments

The targets used in these experiments were CH shells of ~450-μm inner radius and 20- and 24-μm shell thickness. Targets with Ti had 2-μm, Ti-doped CH (6.2% by atom) layers at the inner part of the shell. Targets were filled with 3 or 15 atm of D_2. Targets were irradiated with 351-nm laser light using the 60-beam OMEGA laser system.[7] Two pulse shapes were used in these experiments: a 1-ns square pulse shape with total on-target energy of about 25 kJ and PS26 with a duration of ~2.5 ns and total on-target energy of about 20 kJ. Beam-smoothing techniques used during these experiments included distributed phase plates[8] (DPP's) and smoothing by spectral dispersion[9] (SSD). The 2-D SSD had an IR bandwidth of 1.25 Å × 1.75 Å, producing a 0.2-THz bandwidth at 351 nm. The estimated illumination uniformity for 60 overlapping OMEGA beams with DPP's and SSD was $\sigma_{\text{rms}} \sim 2.5\%$, which was calculated from the on-target single-beam distribution and averaged over the length of the pulse.[10] Beam-to-beam energy variations were typically ~7%, which produces an additional on-target illumination nonuniformity of $\sigma_{\text{rms}} \sim 2.5\%$, with most of that contribution in modes 1 through 5.[10]

The thin solid line in Fig. 83.8 shows the measured spectrum of the core emission integrated over the time of a stagnation phase at peak compression (~300 ps) and integrated over the area of the core (~80 μm). The spectrum is from the implosion of a 24-μm-thick shell, with a 2-μm inner Ti-doped layer and an initial D_2 fill pressure of 3 atm by 1-ns-square-pulse illumination. The spectrum was measured with a spectrometer fitted with an ammonium dihydrogen phosphate (ADP) crystal and a 15-μm-wide slit. The spectrum contains absorption lines due to 1*s*–2*p* transitions in Ti ions near the 4.6-keV energy.[11] These lines are absorbed within the warm Ti-doped region (T ~ 300 to 600 eV), whereas radiation above the Ti *K* edge at 4.96 keV is absorbed by much colder Ti. The intensity above the *K* edge falls down gradually rather than abruptly, indicating a temperature gradient in the absorbing region and an associated gradual *K*-edge shift to higher energies due to ionization.[11] The electron temperature of the emission region ($T_e = 0.86\pm0.04$ keV) and the areal density of cold Ti in the shell ($\rho R_{\mathrm{Ti}} = 2.1\pm0.1$ mg/cm^2) have been derived from the fit to the measured spectrum, shown by the thick solid line outside absorption areas of warm Ti (at ~4.6 keV) and shifted *K* edge.

This spectrum was used not only to identify the spectral regions of x rays appropriate for imaging but also to calculate imaging sensitivity in order to convert intensity modulations in the image to modulations of the shell's areal density.

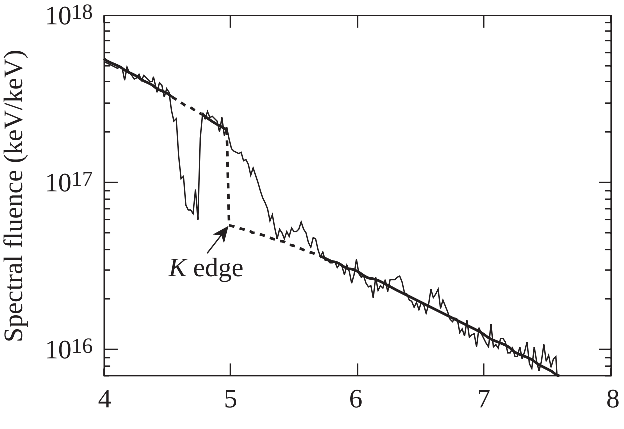

Figure 83.8
Measured time-integrated spectrum of the core emission taken with a 24-μm-thick shell with a 2-μm inner Ti-doped layer, at an initial fill pressure of 3 atm D_2, and 1-ns-square-pulse illumination.

Imaging of Cold-Shell Modulations

To measure the shell's integrity, the target is imaged at energies weakly absorbed by the shell, below the Ti *K* edge, and at energies strongly absorbed by the shell (above the Ti *K* edge at about 6.5 keV). The compressed core radiation serves as a backlighter for the shell.[5] Any modulations in this emission are measured from the core image below the *K* edge. The image above the *K* edge has approximately the same modulations in the backlighter and additional modulations in the absorbing shell.

Time-integrated images of core emission were taken with a 6-μm pinhole array, at 4× magnification, and recorded on DEF film. Two images were taken with a Ti filter at energies below the Ti *K* edge (~4.9 keV); the other two images were taken with an iron filter at energies above the Ti *K* edge (~6.5 keV). A schematic of the instrument is shown in Fig. 83.9. Instead of one image per energy channel, a pair of images were taken not only to reduce noise by averaging images but also to estimate the noise itself by subtracting one image from another. The calculated resolution for the imaging system was ~6 μm, with modulation transfer functions (MTF's) very similar for both 4.9- and 6.5-keV energy channels. The noise spectrum has been used in the Wiener filter applied to reduce noise during image processing. The thicknesses of both the Ti and the Fe filters were varied for different shots in order to achieve an optimum intensity on the film since intensity levels were different for different shot conditions.

The energy spectrum was measured for each target experiment using the crystal spectrometer. The approximate x-ray energy spectra of the images for each energy channel were calculated by multiplying this spectrum by the filter response. Figure 83.10(a) shows the spectra calculated for the lower-energy filter (solid line) and the higher-energy filter (dotted line). The conditions of the target experiment were a 20-μm-thick CH shell with a 2-μm inner Ti-doped layer, filled with 3 atm of D_2, irradiated by a 1-ns square pulse. Lineouts of two lower-energy-band images (solid lines) and two higher-energy-band images (dotted lines) are shown in Fig. 83.10(b). Note that the lineouts from the same energy band have similar features that are different from the features in the other energy band. This indicates that the features seen in the images are not noise, and that the differences between the images at different energies are likely due to modulations in the absorbing shell. (It is assumed that the core-emission image does not change appreciably over an ~1.6-keV interval in photon energy between the two energy bands, i.e., the features of the core

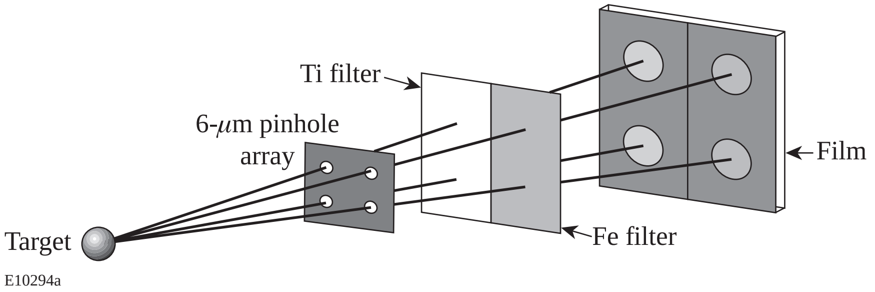

Figure 83.9
Schematic of the 6-μm filtered pinhole array. Two time-integrated images are obtained with a Ti filter at energies below the Ti *K* edge (~4.9 keV); the other two images are obtained with an Fe filter at energies above the Ti *K* edge (~6.5 keV). The magnification of the images is 4× and the images are recorded with DEF film.

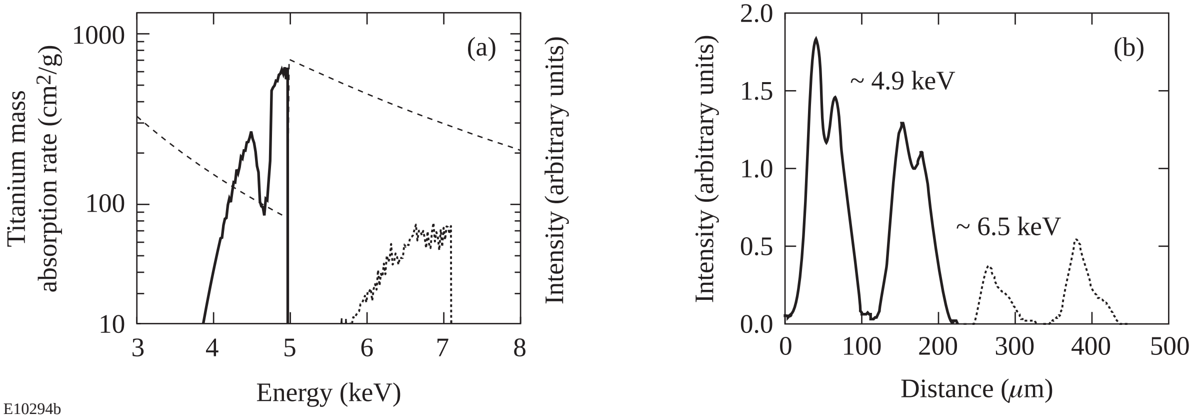

Figure 83.10
(a) The calculated spectra of the images below the Ti *K* edge (solid line) and above the Ti *K* edge (dotted line). The Ti mass absorption rate is shown by the dashed line. (b) The lineouts of two images taken below the Ti *K* edge (solid line) and above the Ti *K* edge (dotted line).

emission are the same at ~4.9 and ~6.5 keV. (This assumption is confirmed in the next section.)

The images were processed with the Wiener-filtering technique.[12] If $C(\mathbf{f})$ is the signal plus noise of the image (obtained by averaging two images for a particular x-ray energy channel) in Fourier space with coordinates $\mathbf{f}$, and $\langle N(\mathbf{f})\rangle$ is the average spectrum of the noise (calculated from the difference of two images for a particular energy band), then the restored signal spectrum $R(\mathbf{f})$ is given by the Wiener-filter formula[12]

$$R(\mathbf{f}) = \frac{C(\mathbf{f})}{\mathrm{MTF}(\mathbf{f})} \bullet \frac{\left|C(\mathbf{f})\right|^2 - \left|\langle N(\mathbf{f})\rangle\right|^2}{\left|C(\mathbf{f})\right|^2}, \tag{1}$$

where $\mathrm{MTF}(\mathbf{f})$ is the modulation transfer function of the pinhole camera calculated for a particular x-ray energy channel. The filtered images are obtained by transforming the restored spectrum $R(\mathbf{f})$ back to real space.

The modulations of the ratio of intensities for filtered images below the *K* edge [$I_{<K}(\mathbf{x})$] and above the *K* edge [$I_{>K}(\mathbf{x})$] are related to the shell-areal-density modulations δ [$rR(\mathbf{x})$] by

$$\delta\left[\rho R(\mathbf{x})\right] = \delta \frac{\left\{\ln\left[\dfrac{I_{<K}(\mathbf{x})}{I_{>K}(\mathbf{x})}\right]\right\}}{\mu_{>K} - \mu_{<K}}, \tag{2}$$

where $\mu_{>K}$ and $\mu_{<K}$ are the spectrally weighed mass absorption coefficients of cold Ti at energies above and below *K* edge, respectively, which were calculated for each shot using the measured x-ray spectra [Fig. 83.10(a)].

Figure 83.11 shows the power per mode of the measured modulation as a function of spatial frequency of the cold, Ti-doped shell areal density at peak compression. The data are from three target experiments, measured using core images taken at x-ray energies above and below the Ti *K* edge. For each target experiment, the areal-density modulations were normalized to the measured cold-shell areal densities, which were deduced from the crystal spectrometer data, similar to that shown in Fig. 83.8, yielding relative modulations in the cold-shell areal density $\delta\left[\rho R(\mathbf{x})\right]/\rho R(\mathbf{x})$. To minimize errors due to spherical effects in the analysis of the outer section of the core images, only the 60-μm-diam central portion of each 100-μm-diam image was analyzed. The spectra in Figs. 83.11(a) and 83.11(b) correspond to 20- and 24-μm-thick-shell targets driven with a 1-ns square pulse shape. The spectrum in Fig. 83.11(c) corresponds to a 24-μm-thick-shell target driven with pulse shape PS26. All three targets were filled with 3 atm of D_2. To obtain the power per mode, shown in Fig. 83.11, absolute values of the Fourier amplitudes squared were summed at each spatial frequency. The $\sigma_{\rm rms}$ of the total nonuniformity is the square root of the sum of the power per mode over the spatial frequency. The spectra shown in Fig. 83.11 are very similar. They are peaked at a spatial frequency of 20 mm^{-1} (corresponding to a wavelength of 50 μm or mode number $\ell \sim 5$) with spatial features extending down to a wavelength of about 15 μm. The total $\sigma_{\rm rms}$ of the nonuniformities is similar for all three shots and is ~50%±20%. Adding previous data[5] to these measurements, we conclude that the nonuniformity $\sigma_{\rm rms}$ ranges from the noise level of ~20% up to ~50% and is similar for target experiments with a 20- or 24-μm-thick shell and with 1-ns square or PS26 pulse shapes.

Measurements of Temperature Nonuniformities

Measurements of the cold-shell integrity are based on the assumption that the distribution of core emission does not change appreciably over an ~1.6-keV interval in photon energy between the two energy bands at ~4.9 and ~6.5 keV. This assumption is valid if the effective emission temperature is constant over the whole area of the image. We use the term "effective" with respect to temperature in order to emphasize that the measured images of the cores are two dimensional, and

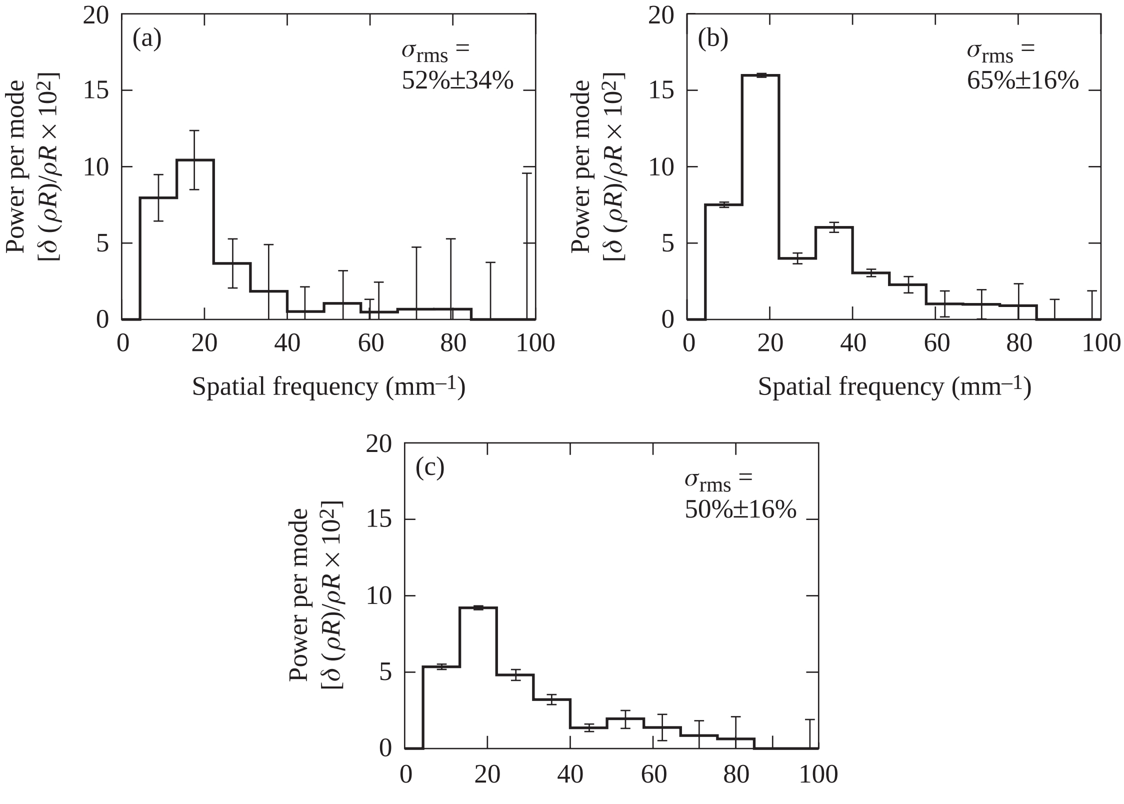

E10057

Figure 83.11
Power per mode of the measured modulation as a function of spatial frequency for target experiments with (a) 20-μm-thick shells and 1-ns square pulse shape, $\sigma_{\rm rms}$ = 52%±34%, (b) 24-μm-thick shells and 1-ns square pulse shape, $\sigma_{\rm rms}$ = 65%±16%, and (c) 24-μm-thick shells and PS26 pulse shape, $\sigma_{\rm rms}$ = 50%±16%. All experiments were taken with 3-atm-D_2-filled shells with a 2-μm-thick, inner-Ti-doped (6.2% by atom) layer.

not three dimensional as the cores are themselves. The intensity at each point is an integral over the core in the direction of the imaging system. Regions with different temperatures may exist inside the core; however, when integrated along the path toward the imaging system, only an integrated or effective temperature is observable.

Figure 83.12 represents the lineouts of the core images measured with Sn filters at an x-ray energy of about 3.5 keV (solid lines) and with Fe filters at an x-ray energy of about 6.5 keV (dashed lines). These data are from a target experiment with a 24-μm-thick CH shell (no Ti doping), filled with 15 atm of D_2 and driven by a 1-ns square pulse shape. At x-ray energies of $\gtrsim$3 keV, the core emission is not significantly absorbed by the outer shell. Differences in the shapes of the images as a function of energy band would indicate the presence of nonuniformities in the effective temperature. Lineouts of the captured images shown in Fig. 83.12 are, in fact, very similar. The image features are similar for the two images taken from the same energy band, indicating that these features are not noise. The fact that these features have the same shape for both energy bands indicates that the effective temperature is nearly constant over the entire area of the images. The measured effective temperature $T_{\text{eff}} = 0.86 \pm 0.04$ keV was found from the ratio of two different energy-band images shown in Fig. 83.12.

A similar analysis was performed on results from experiments with other conditions, including different CH-shell thicknesses and different pulse shapes. For all of these shots effective temperatures were constant over the whole area of the images within the experimental error determined by the noise in the images.

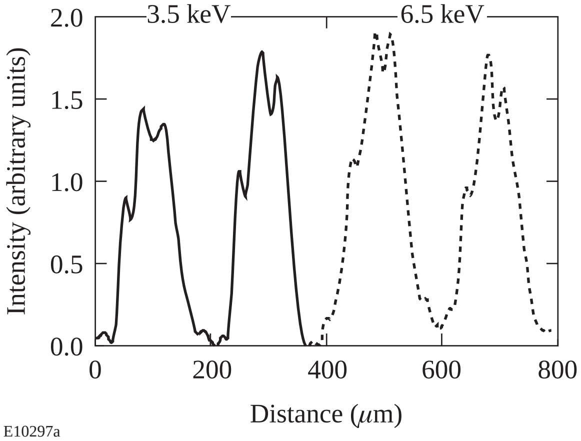

E10297a

Figure 83.12
The lineouts of two images taken at ~3.5 keV (solid line) with a Sn filter, and at ~6.5 keV (dashed line) with an Fe filter for a target experiment on a 24-μm-thick shell, filled with 15 atm of D_2, driven by a 1-ns square pulse shape.

Imaging the Hot-Shell Modulations

As shown above, the core images have no temperature nonuniformities within the experimental resolution and sensitivity; the modulations seen in the high-energy, unattenuated images are due to areal-density modulations in the emission region. The core images are produced by the emission from the hot core and dominated by the emission from the inner hot shell; therefore, modulations in the image lineouts shown in Fig. 83.12 are mostly due to hot-shell areal-density modulations. Assuming that the absorption of x rays in the core and the shell is negligible, the intensity at the detector is proportional to the areal density of the emission region in the direction of x-ray propagation.

To analyze the areal-density nonuniformity of the hot inner shell, the smooth envelope of the core image $I_{\text{env}}(\mathbf{x})$ (obtained by filtering the image in Fourier space) was subtracted from the core image $I(\mathbf{x})$. The relative areal-density nonuniformity of the hot shell is given by the relation

$$\frac{\delta[\rho R(\mathbf{x})]}{\rho R(\mathbf{x})} = \sqrt{2}\left(\frac{I(\mathbf{x}) - I_{\text{env}}(\mathbf{x})}{I_{\text{env}}(\mathbf{x})}\right). \tag{3}$$

Since the signals from both "walls" of the hot shell are added to give $I(\mathbf{x})$, the relative nonuniformities in the captured image $[I(\mathbf{x}) - I_{\text{env}}(x)]/I_{\text{env}}(\mathbf{x})$ are multiplied by the factor of $\sqrt{2}$ in order to analyze modulations corresponding to only one wall of the shell (the assumption made here was that areal-density perturbations in the shell region are uncorrelated).

Figure 83.13 shows the measured power per mode of the areal-density nonuniformities as a function of spatial frequency for the hot inner shell. The spectrum is peaked at spatial scale lengths of 40 to 50 μm with a total σ_{rms} of 30%±15%. It is similar to the measured cold-shell spectra in both magnitude and shape.

Conclusions

Time-integrated measurements of the shell integrity are presented at peak compression, the final stage of a spherical implosion. Perturbations in the cold, or absorbing, part of the shell were studied using shells with and without inner Ti-doped layers. The hot, or emitting, part of the shell was studied using pure plastic shells. It is found that modulations in both

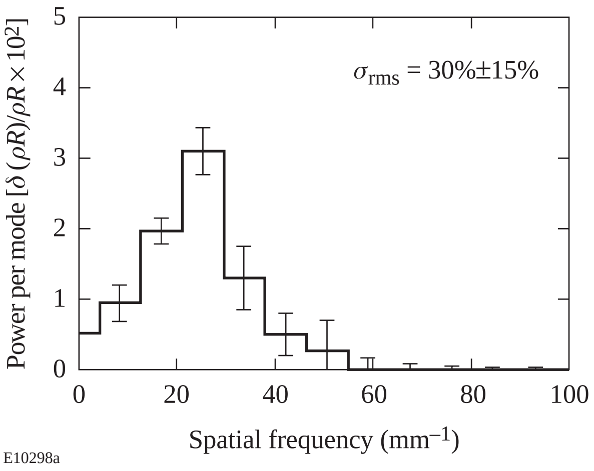

Figure 83.13
Power per mode of hot CH plasma emission as a function of spatial frequency for a target experiment on a 24-μm-thick shell, filled with 15 atm of D_2, driven by a 1-ns square pulse shape, σ_{rms} = 30%±15%.

the cold and hot parts of the shell are peaked at spatial scale sizes of 40 to 50 μm, with nonuniformities extending to ~15 μm. The magnitude of relative areal-density perturbations is in the range from the noise level of ~15% to 20% up to ~50% for both 1-ns square and PS26 pulse shapes. Time-resolved measurements at peak compression and earlier, in the deceleration phase, will aid in understanding the present findings.

ACKNOWLEDGMENT

This work was supported by the U.S. Department of Energy Office of Inertial Confinement Fusion under Cooperative Agreement No. DE-FC03-92SF19460, the University of Rochester, and the New York State Energy Research and Development Authority. The support of DOE does not constitute an endorsement by DOE of the views expressed in this article.

REFERENCES

1. S. E. Bodner, D. G. Colombant, J. H. Gardner, R. H. Lehmberg, S. P. Obenschain, L. Phillips, A. J. Schmitt, J. D. Sethian, R. L. McCrory, W. Seka, C. P. Verdon, J. P. Knauer, B. B. Afeyan, and H. T. Powell, Phys. Plasmas **5**, 1901 (1998).
2. J. D. Lindl, Phys. Plasmas **2**, 3933 (1995).
3. D. K. Bradley, J. A. Delettrez, R. Epstein, R. P. J. Town, C. P. Verdon, B. Yaakobi, S. Regan, F. J. Marshall, T. R. Boehly, J. P. Knauer, D. D. Meyerhofer, V. A. Smalyuk, W. Seka, D. A. Haynes, Jr., M. Gunderson, G. Junkel, C. F. Hooper, Jr., P. M. Bell, T. J. Ognibene, and R. A. Lerche, Phys. Plasmas **5**, 1870 (1998).
4. B. Yaakobi, F. J. Marshall, D. K. Bradley, J. A. Delettrez, R. S. Craxton, and R. Epstein, Phys. Plasmas **4**, 3021 (1997).
5. B. Yaakobi, V. A. Smalyuk, J. A. Delettrez, R. P. J. Town, F. J. Marshall, V. Yu. Glebov, R. D. Petrasso, J. M. Soures, D. D. Meyerhofer, and W. Seka, in *Inertial Fusion Sciences and Applications '99*, edited by W. J. Hogan C. Labaune, and K. A. Tanaka (Elsevier, Paris, 2000), pp. 115–121.
6. B. Yaakobi, F. J. Marshall, and D. K. Bradley, Appl. Opt. **37**, 8074 (1998).
7. T. R. Boehly, D. L. Brown, R. S. Craxton, R. L. Keck, J. P. Knauer, J. H. Kelly, T. J. Kessler, S. A. Kumpan, S. J. Loucks, S. A. Letzring, F. J. Marshall, R. L. McCrory, S. F. B. Morse, W. Seka, J. M. Soures, and C. P. Verdon, Opt. Commun. **133**, 495 (1997).
8. Y. Lin, T. J. Kessler, and G. N. Lawrence, Opt. Lett. **20**, 764 (1995).
9. S. Skupsky, R. W. Short, T. Kessler, R. S. Craxton, S. Letzring, and J. M. Soures, J. Appl. Phys. **66**, 3456 (1989).
10. F. J. Marshall, J. A. Delettrez, V. Yu. Glebov, R. P. J. Town, B. Yaakobi, R. L. Kremens, and M. Cable, Phys. Plasmas **7**, 1006 (2000).
11. B. Yaakobi, R. S. Craxton, R. Epstein, and Q. Su, J. Quant. Spectrosc. Radiat. Transfer **58**, 75 (1997).
12. V. A. Smalyuk, T. R. Boehly, D. K. Bradley, J. P. Knauer, and D. D. Meyerhofer, Rev. Sci. Instrum. **70**, 647 (1999); W. H. Press *et al.*, *Numerical Recipes in FORTRAN: The Art of Scientific Computing*, 2nd ed. (Cambridge University Press, Cambridge, England, 1992), pp. 701–715.